SEPT9: From pan-cancer to lung squamous cell carcinoma

Wenwen Wang[1†], Xiaochen Zhang[2†], Ping Gui[3], Qizhen Zou[1], Yuzhou Nie[4], Shenglin Ma[5] and Shirong Zhang[1*]

Abstract

Background *SEPT9* is a pivotal cytoskeletal GTPase that regulates diverse biological processes encompassing mitosis and cytokinesis. While previous studies have implicated *SEPT9* in tumorigenesis and development; comprehensive pan-cancer analyses have not been performed. This study aims to systematically explore its role in cancer screening, prognosis, and treatment, addressing this critical gap.

Methods Gene and protein expression data containing clinical information were obtained from public databases for pan-cancer analyses. Additionally, clinical samples from 90 patients with lung squamous cell carcinoma (LUSC) were used to further experimentally validate the clinical significance of SEPT9. In addition, the molecular docking tool was used to analyze the affinities between SEPT9 protein and drugs.

Results *SEPT9* is highly expressed in various cancers, and its aberrant expression correlates with genetic alternations and epigenetic modifications, leading to adverse clinical outcomes. Take LUSC as an example, additional dataset analyses and immunohistochemical experiments further confirm the diagnostic and prognostic values as well as the clinical relevance of the *SEPT9* gene and protein. Functional enrichment, single-cell expression, and immune infiltration analyses revealed that *SEPT9* promotes malignant tumor progression and modulates the immune microenvironments, enabling patients to benefit from immunotherapy. Moreover, drug sensitivity and molecular docking analyses showed that *SEPT9* is associated with the sensitivity and resistance of multiple drugs and has stable binding activity with them, including Vorinostat and OTS-964. To harness its prognostic and therapeutic potential in LUSC, a mitotic spindle-associated prognostic model including *SEPT9*, *HSF1*, *ARAP3*, *KIF20B*, *FAM83D*, *TUBB8*, and several clinical characteristics, was developed. This model not only improves clinical outcome predictions but also reshapes the immune microenvironment, making immunotherapy more effective for LUSC patients.

Conclusion This is the first study to systematically analyze the role of *SEPT9* in cancers and innovatively apply the mitotic spindle-associated model to LUSC, fully demonstrating its potential as a valuable biomarker for cancer screening and prognosis, and highlighting its application value in promoting immunotherapy and chemotherapy, particularly for LUSC.

Keywords Drug therapy, Immunotherapy, LUSC, Prognostic model, *SEPT9*, Tumor immune microenvironment

---

†Wenwen Wang and Xiaochen Zhang contributed equally to this work.

*Correspondence:
Shirong Zhang
shirleyz4444@163.com
Full list of author information is available at the end of the article

Wang *et al. BMC Cancer*   (2024) 24:1105

Page 2 of 20

Background

Cancer is the disease with the highest incidence and mortality worldwide, and its etiology and treatment remain a concerning issue. The latest global cancer statistics report that lung cancer has once again replaced breast cancer as the most common and deadly type of cancer, making the diagnosis and treatment of lung cancer more urgent [1]. Current cancer research should focus on the origin of tumor cells, especially their local microenvironment, to elucidate new carcinogenic mechanisms that will guide the development of drugs and new treatment methods. However, innovative treatment strategies are rarely beneficial to all patients, and the continued emergence of drug resistance makes cancer treatment more challenging [2–4]. Therefore, new sensitive biomarkers for early cancer screening and treatment planning are urgently needed.

Septins (*SEPTs*) represent a highly conserved cytoskeletal GTPase family widely present in eukaryotes and participate in various biological processes including cell polarization, migration, cytoplasmic division, and membrane remodeling [5, 6]. In mammals, 13 SEPT subunits have been identified; they are subdivided into four subgroups based on their structure and function: SEPT2 (1, 2, 4, 5), SEPT3 (3, 9, 12), SEPT6 (6, 8, 10, 11, 14), and SEPT7 [7]. These proteins not only interact with each other, but also bind extensively to other cytoskeletal components (including microtubules, microfilaments, and intermediate fibers); thus, SEPTs are considered to be the fourth type of cytoskeleton [8]. However, due to the unique structure and complex functions of SEPT members, this novel cytoskeleton remains mysterious.

SEPT9 is located at both ends of the core octamer SEPT9-7–6-2–2-6–7-9 to promote the assembly of SEPT subunits, which is crucial for maintaining the stability of the overall SEPT structure. In recent years, an increasing number of studies have linked SEPT9 to pathological processes including tumorigenesis and development, pathogenic microbial infections, and neurological diseases, particularly tumors. Aberrant expression or mutation of *SEPT9* hinders the assembly of mitotic spindles and the formation of cytoplasmic separation contraction loops, cell cycle dysregulation and aneuploidy, a major cause of tumorigenesis [9–12]. Malignant tumors typically contain different *SEPT9* isoforms. For example, isoforms v2, v4, v4*, and v5 show high expression levels in the epithelium of colorectal cancer (COADREAD), whereas v1 exhibits high expression levels in the normal epithelium [13]; isoforms v1 and v4 dominate in the epithelium of ovarian cancer [14]. Furthermore, the *SEPT9* isoforms exhibit varying expression levels in distinct cellular compartments. For example, the nucleus of breast cancer mainly expresses isoform v1 [15]. Elevated levels of *SEPT9*

encourage the growth, migration, invasion, and metastasis of cancer cells, prevent cell apoptosis, and are linked to unfavorable patient outcomes [16, 17]. Conversely, low *SEPT9* expression is associated with epigenetic modifications, especially high methylation in the promoter region, which inhibits its expression and hinders cytoplasmic division, autophagy, and DNA repair, thereby promoting tumorigenesis, epithelial-mesenchymal transition (EMT), and metastasis. At present, *SEPT9* methylation has been clinically proven to be a highly specific biomarker for the early screening of COADREAD [18, 19]. In addition, abnormal *SEPT9* methylation has also been found in LIHC, breast cancer, and HNSC [20–22]. Therefore, the study of *SEPT9* is crucial for the diagnosis and treatment of cancer. However, there is currently a lack of comprehensive analyses of *SEPT9*.

In the present study, we systematically analyzed the expression and clinical significance of *SEPT9* in cancer, especially in LUSC. We aimed to construct a *SEPT9*-based mitotic spindle-associated prognostic model and evaluated its potential in predicting clinical outcomes and immunotherapy efficacy in LUSC patients. Figure 1 presents the flowchart of our study.

Methods

Data collection

All RNA sequencing and chip data with clinical information of tissues were sourced from the Cancer Genome Atlas (TCGA, https://portal.gdc.cancer.gov/), University of California Santa Cruz (UCSC) XENA (https://xena.ucsc.edu/), and Gene Expression Omnibus (GEO, https://www.ncbi.nlm.nih.gov/geo/) databases. RNA sequencing data for cancer cell lines were derived from the Dependency Map (DepMap) portal (https://depmap.org/portal/). Gene transcript information was obtained from the Ensembl portal (https://feb2023.archive.ensembl.org/index.html). RNA expression of single-cells in normal tissues, and protein information including expression, subcellular localization, and structural prediction, were obtained from the Human Protein Atlas (HPA) portal (https://www.proteinatlas.org/). Genetic alternation, DNA methylation, and protein posttranslational modification (PTM) data were obtained from cBioPortal (https://www.cbioportal.org/) [23], Shiny Methylation Analysis Resource Tool (SMART) portal (http://www.bioinfo-zs.com/smartapp/) [24], and PhosphoSitePlus portal (6.7.4, https://www.phosphosite.org/homeAction) [25], respectively. All the data were collected between February and March 2024 and statistically analyzed and visualized using R software (4.3.2, https://cran.r-project.org/bin/windows/base/old/4.3.2/) with the ggplot2 package (3.5.0). Other packages were downloaded from the R portal (https://cran.r-project.org/web/packages/) or Bioconductor portal (https://www.bioconductor.org/).

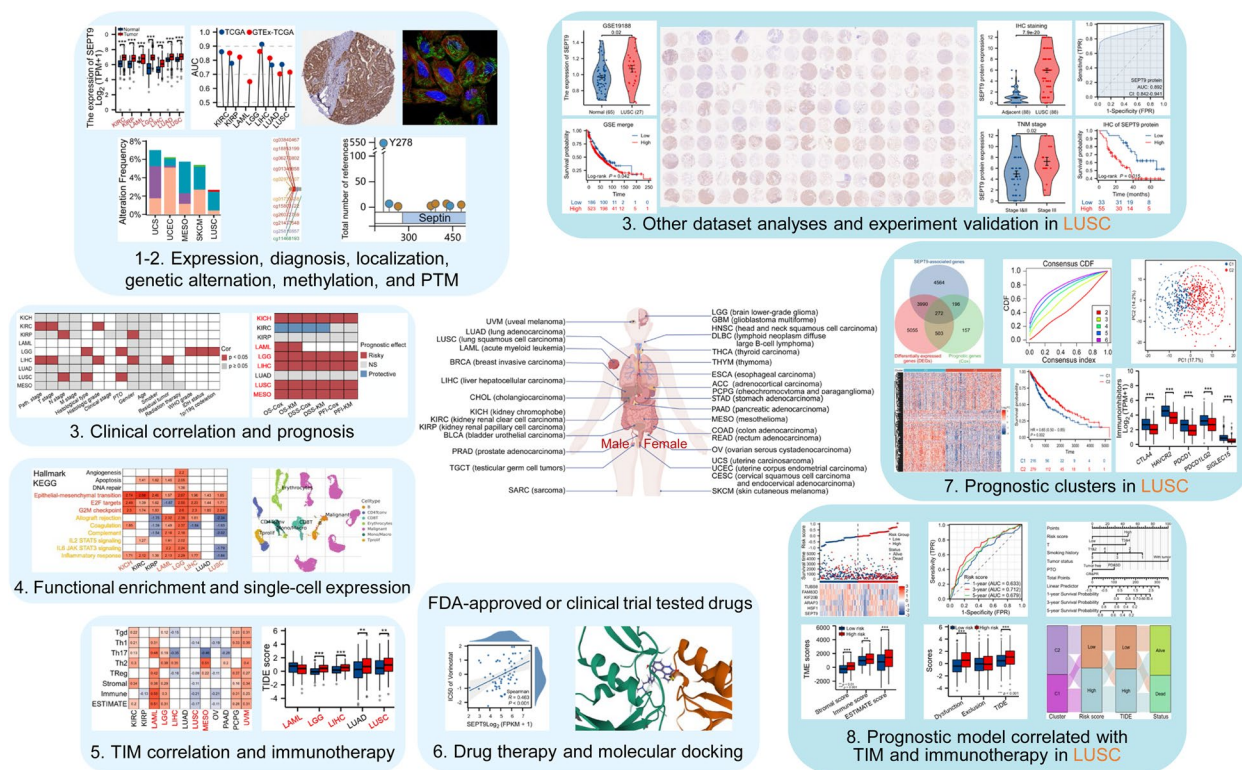Wang *et al. BMC Cancer*   (2024) 24:1105

Page 3 of 20

Fig. 1 Flowchart of the study

Differential, correlation, diagnostic, and prognosis analyses

Differential analyses, including mRNA and protein expression, methylation, infiltration, and score analyses, were conducted using the stats (4.2.1) and car (3.1–0) packages and visualized using box or violin plots.

Correlation analyses, including SEPT9 mRNA or protein with CNV, methylation, clinical factors, immune infiltration, drugs, mitotic spindle genes, as well as clusters, scores, and survival status analyses, were conducted using Spearman's method and visualized using scatter plots, heatmaps, or Sankey plots. Baseline correlation analyses of *SEPT9* and clinical factors were conducted using the stats (4.2.1) package and visualized using heatmaps. Only significant correlations ($p < 0.05$) were displayed on the heatmaps. The correlations between groups are presented as Sankey plots using ggalluvial package (0.12.5).

Diagnostic analyses, including the determination of normal and tumor tissues, as well as the patient status, were performed using the pROC (1.18.5) and timeROC (0.4) packages and visualized using lollipop plots or Receiver operating characteristic (ROC) curves.

Prognostic analyses, including overall survival (OS), progress-free interval (PFI), and disease-specific survival (DSS), were performed using the surviving (0.3.0) and

survminer (0.4.9) packages and visualized using Kaplan–Meier (KM) plots or heatmaps.

Immunohistochemical assays on tissue microarrays

The microarray (HLugS180Su02, Outdo Biotech, China) consisted of 90 pairs of adjacent and LUSC tissue samples containing clinical information produced into 4-μm thick paraffin-embedded frozen sections. Immunohistochemical (IHC) staining was performed using SEPT9 antibodies (HPA042564, Atlas Antibodies, Sweden), and images were acquired using an Aperio XT scanner (Leica). Image analyses with staining scores (0–12) were assigned by multiplying the staining intensity (0–3) by area (0–4). Owing to issues of sample shedding and uneven staining, 176 cases of adjacent (88) and LUSC (88) samples were ultimately included in the statistics. All experimental procedures were performed according to standardized protocols [26].

Functional enrichment analyses

Differentially expressed genes (DEGs) were identified between high- and low-*SEPT9* groups in pan-cancer using the edgeR package (3.38.2) and then analyzed with Gene Set Enrichment Analysis (GSEA) using the clusterProfiler package (4.10.1) with hallmark gene sets and visualized with a heatmap. Only normalize enrichment score (NES) with a significant difference (adjusted $p < 0.05$) are shown.

Wang *et al. BMC Cancer*   (2024) 24:1105

Page 4 of 20

Single-cell expression analyses

ScRNA-seq data from the GEO database were analyzed through the Tumor Immune Single-cell Hub (TISCH1, http://tisch1.comp-genomics.org/, accessed on 4 March, 2024), a portal dedicated to TIM [27]. *SEPT9* levels in various cell types across different TIM were displayed through heatmap and violin plots, while its distribution in different cell clusters was visualized using Uniform Manifold Approximation and Projection (UMAP) plots.

TIM infiltration analyses and immunotherapy prediction

TIM infiltration includes stromal and immune cell infiltration, which correspond to stromal and immune scores, respectively, the sum of which is the estimate or tumor microenvironment (TME) score. Infiltration analyses were performed using the GSVA (1.34.0) package with the ssGSEA method, estimate (1.0.13) packages, and immunedeconv package with the xCell method. The status of the cancer immune cycle, including seven different antitumor immune statuses from cancer antigen release (step one) to cancer cell killing (step seven), was analyzed using the Tracking Tumor ImmunoPhenotype portal (TIP, http://biocc.hrbmu.edu.cn/TIP/, accessed on 3 February, 2024) [28].

Immune checkpoint blockade (ICB) efficacy was predicted mainly using the Tumor Immune Dysfunction and Rejection (TIDE, http://tide.dfci.harvard.edu/, accessed on 4 February, 2024) portal to evaluate two types of immune escape: dysfunction of cytotoxic T lymphocytes and expression of immunosuppressive factors. Higher TIDE scores suggest stronger immune evasion, resulting in reduced effectiveness of ICB [29, 30].

Drug sensitivity and molecular docking analyses

Drug sensitivity analyses were based on the relationship of gene expression with the half-maximal inhibitory concentration (IC50) of drugs. The processed datasets including RNA expression and drug activity in NCI-60 cancer cell lines were obtained from the CellMiner portal (https://discover.nci.nih.gov/cellminer/, accessed on 27 March, 2024), and Food and Drug Administration-approved or clinical trial-tested drugs were extracted using the impute (1.76.0) and limma (3.58.1) packages for further analysis [31]. Positive correlations indicate that higher gene expression may lead to drug resistance, whereas negative correlations indicate drug sensitivity.

To analyze the interaction modes and binding affinities between protein and potential drugs, SEPT9 and drug structures were downloaded from the protein data bank (PDB, https://www.rcsb.org/) (ID: 5CYO; resolution: 2.04 Å) and PubChem Compounds portal (https://pubchem.ncbi.nlm.nih.gov/), respectively, and molecular docking was performed using Autodock Vina 1.2.2 software, a silico protein–ligand docking software [32, 33].

Establishment and evaluation of prognostic clusters, risk signature, and nomogram

SEPT9-associated genes (Spearman Cor > 0.1, $p < 0.05$), DEGs between normal and LUSC tissues ($|\log_2$fold change| > 0.58, $p < 0.05$), and prognostic genes in LUSC ($p < 0.05$) were identified using the Spearman correlation method, edge package (2.34.0), and survival package (3.5.8), respectively. The shared genes were displayed on Venn diagrams using the VennDiagram package (1.7.3). Patient clustering was performed using the Consensus-ClusterPlus package (1.66.0), followed by cumulative distribution function (CDF) to obtain the appropriate clustering method. Distribution differences among clusters were determined using principal component analysis (PCA).

The collection of human mitotic spindle genes was compiled by combining the HALLMARK_MITOTIC_SPINDLE (2023.2) and GOCC_MITOTIC_SPINDLE (2023.2) gene sets from the Molecular Signatures Database (MSigDB, https://www.gsea-msigdb.org/gsea/msigdb/). The risk signature was constructed by using multivariate Cox regression with the survival package (3.5.8) to identify independent prognostic genes among *SEPT9*-associated prognostic DEGs and mitotic spindle genes. The risk score calculation was obtained using the ggrisk package (1.3).

Uni- and multi-variate Cox regression analyses were used to screen independent factors from the risk signature and clinical factors to construct the prognostic model, and the results are displayed as forest plots. A nomogram was developed based on these independent factors ($p < 0.05$) using the rms (6.8–0) and survival packages. Its accuracy was evaluated through calibration curves, and its clinical net benefit was evaluated with Decision curve analysis (DCA) using survival package and stdca document.

Results

High SEPT9 expression serves as a screening factor for various cancers

To explore the impact of *SEPT9* on tumorigenesis, we conducted pan-cancer data collection and analyses. We found that *SEPT9* was encoded by chromosome 17q25.3 (Fig. 2A), with a total of 48 distinct transcripts (Fig. S1A), and was widely present in various healthy tissues, especially lymphoid tissue and bone marrow, including the thymus, lymph node, and spleen (Fig. 2B). Further single-cell expression analyses of these tissues revealed that *SEPT9* was enriched in immune cells, particularly monocytes, dendritic, T, NK, B, and Kupffer cells (Fig. 2C). Compared with normal tissues, *SEPT9* expression was

Wang *et al. BMC Cancer*   (2024) 24:1105

Page 5 of 20

high in most tumor tissues but low in PRAD (Fig. 2D). Detailed cancer cell line analyses revealed that *SEPT9* expression was highest in Vater, fibroblasts, and skin cells (Fig. 2E). Diagnostic analysis indicated that *SEPT9* had relatively high diagnostic values (area under curve [AUC] > 0.7) for BRCA, CHOL, DLBC, ESCA, GBM, HNSC, KIRC, KIRP, LGG, LIHC, LUAD, LUSC, STAD, THCA, and THYM (Fig. 2F).

Next, we investigated the expression of SEPT9 protein. The predicted SEPT9 structure consisted of an amino-terminal composed of random coils and a carboxyl-terminal containing multiple alpha-helices and beta-strands (Fig. 2G). Immunofluorescence showed that SEPT9 was mainly located in the cytoplasm as actin filaments and occasionally on the cell membrane (Fig. 2H). In line with mRNA levels, IHC images revealed elevated SEPT9 protein levels in BRCA, GBM, LUAD, LUSC, OV, SKCM, and THCA (Fig. 2I, J; Fig. S1B). Collectively, *SEPT9* is highly expressed in various cancers, highlights its crucial role in early cancer screening.

SEPT9 expression is influenced by its genetic alterations, epigenetic modifications, and PTMs

Gene expression is influenced by various factors, including genetic alterations and epigenetic factors. Therefore, we first analyzed the genetic alterations of *SEPT9* in pan-cancer, including simple nucleotide variation (mutations), structural variations, copy number variation (CNVs; including deep deletions and amplifications), and multiple alterations. Genetic alterations occurred in 27 tumor types, particularly UCS, UCEC, MESO, and SKCM (> 5%). Mutations, particularly in UCEC (5.1%), SKCM (2.7%), and STAD (2.27%), as well as copy number amplifications (CNAs), particularly in BRCA (3.78%), LIHC (3.76%), and MESO (3.45%), were dominant, while deep deletions and multiple alterations occurred less frequently (< 1.3%) (Fig. 3A). Mutation analyses indicated that 114 out of 10,953 individuals had mutations, of which 92 were missense, 14 were fusions, six were truncations, and two were splices. Among them, the frequency of lysine-to-arginine conversion at position 298 was the highest, including two patients with UCEC and one with STAD (Fig. 3B). Given that CNVs are closely related to gene expression,

we further analyzed their correlation with *SEPT9* expression. Except for LAML, *SEPT9* positively correlated with CNVs in most tumors, particularly UCS, TGCT, and ESCA (Fig. 3C; Table S1). Survival analyses showed that the genetic alteration of COADREAD patients resulted in shorter OS than those in the unaltered group (Fig. 3D).

SEPT9 expression is also influenced by epigenetic characteristics, particularly DNA methylation. A total of 134 methylation sites were identified in *SEPT9* (Fig. 3E). Compared with normal tissues, CpG-aggregated methylation was increased in BLCA, BRCA, CESC, COAD, ESCA, HNSC, LIHC, PRAD, READ, and UCEC and downregulated in CHOL, KIRC, LUAD, PAAD, and THCA (Fig. 3F). In addition, except for TGCT and THYM, *SEPT9* expression was negatively correlated with methylation (Fig. 3G; Table S2). High CpG-aggregated methylation was a risk factor in ACC, KIRP, and LUAD, whereas GBM, LGG, MESO, THYM, and UVM showed the opposite trend (Fig. 3H).

Furthermore, we explored the PTMs of the SEPT9 protein and found 82 modified sites, including phosphorylation, acetylation, ubiquitylation, and other modifications. Among them, phosphorylation of tyrosine at position 278 was the most frequently mentioned, followed by S30, T49, S85, and T42, indicating that the phosphorylation of SEPT9 at these sites may be important for tumorigenesis and progression (Fig. 3I). Collectively, *SEPT9* expression is impacted by genetic alterations, epigenetic modifications, and PTMs.

SEPT9 correlates with clinical factors and is an effective prognostic factor for various cancers, especially LUSC

Subsequently, the clinical correlation and significance of *SEPT9* expression were analyzed and validated. *SEPT9* was associated with multiple clinical factors in various cancers, except for BRCA, CHOL, LAML, LUAD, MESO, OV, SKCM, and UVM (Fig. 4A, B; Table S3, 4). Next, to further explore the impact of *SEPT9* expression on the outcomes of cancer patients, we analyzed their survival data using Cox regression and log-rank p methods. Elevated levels of *SEPT9* in KICH, LAML, LGG, LIHC, LUSC, MESO, and UVM were associated with decreased OS, PFI, and DSS (Fig. 4C; Fig. S2; Table S5).

(See figure on next page.)

Fig. 2 High *SEPT9* expression serves as a screening factor for various cancers. (**A**) Genomic position of *SEPT9*. (**B**) *SEPT9* expression in healthy tissues from GTEx or HPA datasets. (**C**) Single-cell expression of *SEPT9* in normal tissues. (**D**) *SEPT9* expression between healthy and tumor tissues from GTEx-TCGA database. (**E**) *SEPT9* expression in cancer cell lines from DepMap portal. (**F**) Diagnostic value of *SEPT9* using ROC method from TCGA and GTEx-TCGA databases. (**G**) The prediction structure of SEPT9 protein with AlphaFold method. Different colors represent the per-residue confidence scores. (**H**) Representative immunofluorescence staining of SEPT9 protein from HPA database. (**I, J**) Representative immunohistochemical staining (I) and statistics (J) of SEPT9 protein consistent with mRNA expression in adjacent and tumor tissue from HPA database
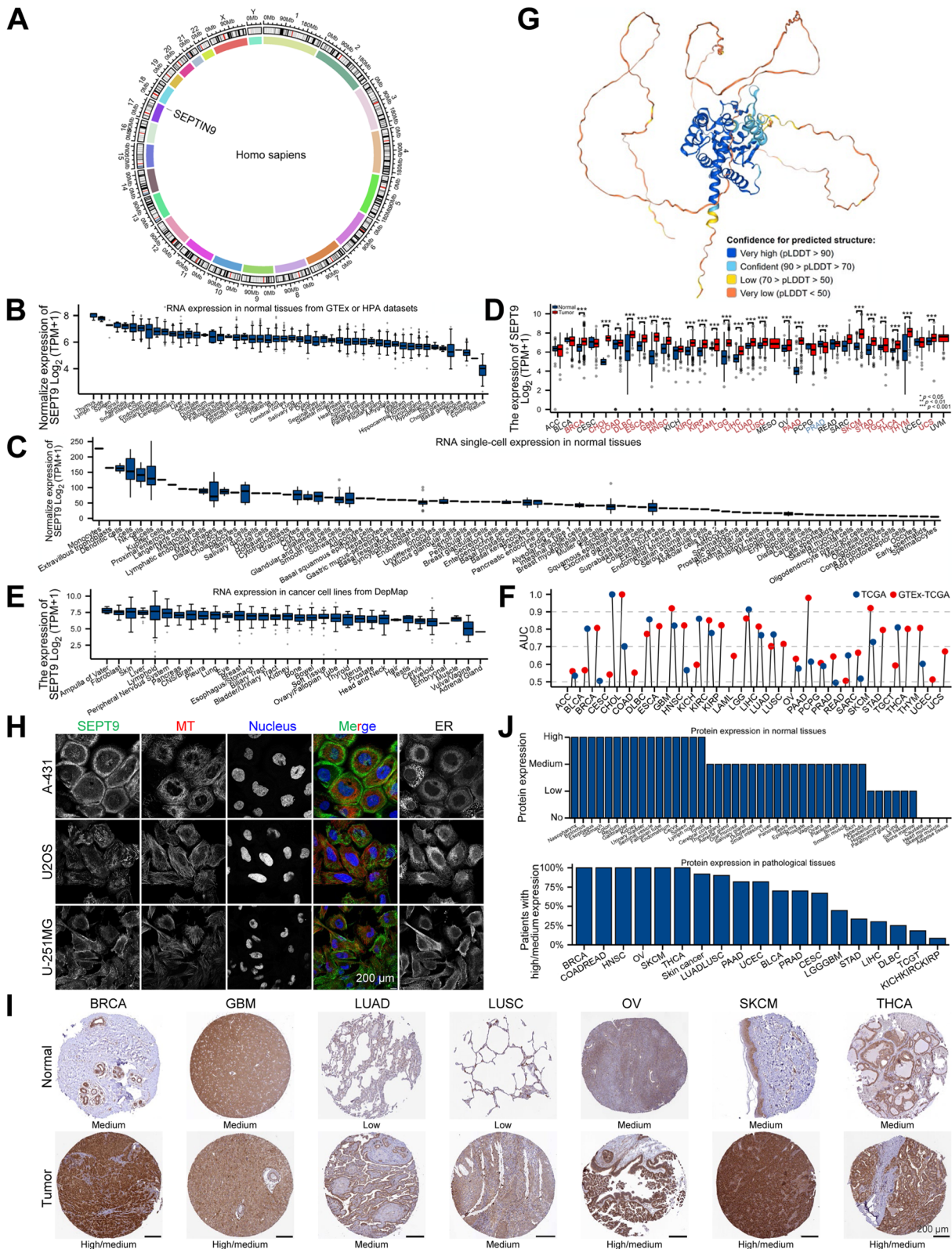
Wang *et al. BMC Cancer* (2024) 24:1105

Page 6 of 20

Fig. 2 (See legend on previous page.)

Given the consistent expression and clinical significance of SEPT9 mRNA and protein, we selected LUSC for further validation. The GSE19188 dataset confirmed the expression and prognostic outcomes of *SEPT9* in LUSC (Fig. 4D), whereas GSE3141 and bulk datasets containing GSE3141, GSE1918, GSE4573, GSE50081, GSE157011, GSE14814, GSE29013, GSE30219, and GSE37745 confirmed the prognostic value of *SEPT9* (Fig. 4E). Importantly, the IHC assay of our collected clinical samples revealed a significant upregulation of SEPT9 protein in LUSC tissues compared to benign ones, indicating high diagnostic value (AUC = 0.892) (Fig. 4F-I). Combined with the clinical information of the patients, SEPT9 protein expression was associated with the TNM stage, PD-L1, and CD68 (Table 1). The stage III, young, and low-CD68 groups showed increased SEPT9 protein levels and vice versa (Fig. 4J; Fig. S3). Patients with higher SEPT9 protein expression had shorter OS time than those with lower expression (Fig. 4K). In summary, *SEPT9* is associated with tumor progression and results in an unfavorable prognosis in specific cancers, particularly LUSC.

SEPT9 is associated with tumor-promoting signature and TIM and is enriched in both malignant and immune cells

We further explored the possible mechanism by which *SEPT9* causes differences in survival. Patients with high *SEPT9* expression exhibited significant enrichments in tumor-promoting hallmarks, including mitotic spindle, EMT, E2F targets, and G2M checkpoint. However, opposite enrichments were observed in immune-related hallmarks, including allograft rejection, coagulation, complement, IL2 STAT5 signaling, IL6 JAK STAT3 signaling, inflammatory response, and interferon-alpha or gamma response. Specifically, positive enrichment was found in ACC, LAML, LGG, PCPG, PRAD, THCA, and UVM, whereas the opposite was observed in DLBC, LUSC, MESO, OV, SARC, SKCM, THYM, UCEC, and UCS. Both types of enrichment were simultaneously observed in CHOL, KIRP, and LIHC (Fig. 5A; Table S6). Together, these results indicated that high *SEPT9* expression promotes the occurrence and progression of most tumors; the regulation of the immune microenvironment varies depending on the cancer type.

As the TCGA sequencing data contained mixed data of not only tumor but also immune, stromal, and other cells, we further utilized single-cell data to observe *SEPT9* expression in specific cell types. In most tumors, *SEPT9* was enriched in both malignant and immune cell clusters (Fig. 5B; Table S7). In acute lymphoblastic leukemia (ALL-GSE132509), *SEPT9* was highly expressed in conventional CD4 T (CD4Tconv), proliferating T (T prolif), CD8T, B, and monocyte/macrophage (Mono/Macro) cells, as well as malignant cells. There were also instances wherein enrichment tended to occur in a particular cell cluster. For example, *SEPT9* tended to be enriched in malignant cell clusters of gliomas-GSE102130, indicating that high *SEPT9* expression was more conducive to the growth of glioma cells in these patients. In contrast, *SEPT9* was only enriched in immune cell clusters of COADREAD-GSE136394, especially CD4Tconv and T prolif, indicating that its high expression was more favorable for the antitumor immune response in these patients (Fig. 5C). Collectively, these results indicated that *SEPT9* is enriched in both malignant and immune cells, and affects the progression of specific tumors by regulating the distribution and function of immune cells.

SEPT9-related TIM is beneficial for predicting immunotherapeutic and chemotherapeutic efficacy

Functional enrichment and single-cell expression analyses suggested that *SEPT9* participates in TIM regulation. Therefore, we conducted comprehensive analyses of the relationship of *SEPT9* with TIM infiltration. *SEPT9* showed negative correlations with the ESTIMATE and TME scores of BRCA, CESC, DLBC, GBM, HNSC, LIHC, LUAD, LUSC, MESO, OV, PRAD, SARC, SKCM, TGCT, UCEC, and UCS, while displaying positive correlation with the scores of KIRC, LAML, LGG, PCPG, THCA, THYM, and UVM. This suggests that *SEPT9* inhibits TIM infiltration in the former set of cancers but enhances the infiltration in the latter. Further analyses of cell types revealed positive correlations between *SEPT9* and infiltration of NK and Th2 cells in almost all tumors, indicating that antitumor immunity represented by NK cells and tumor suppression represented by Th2 cells jointly regulate *SEPT9*-associated TIM (Fig. 6A, B; Table S8). Next, we analyzed the effect of *SEPT9* expression on the cancer-immune cycle, which can be divided

(See figure on next page.)

Fig. 3 *SEPT9* expression is impacted by its genetic alterations, epigenetic modifications, and PTMs. (**A**) The frequency of *SEPT9* genetic variation from cBioPortal. (**B**) Mutation diagram of *SEPT9*. (**C**) Correlations of *SEPT9* with CNVs. (**D**) OS of *SEPT9* genetic alteration. (**E**) Detailed chromosomal distribution of methylation probes from SMART portal. (**F**) CpG-aggregated methylation between normal and tumor tissues. Aggregation method: median; methylation value: beta-value. (**G**) Correlations of *SEPT9* with CpG-aggregated methylation. (**H**) OS of CpG-aggregated *SEPT9* methylation. (**I**) PTMs of SEPT9 protein from PhosphoSitePlus portal

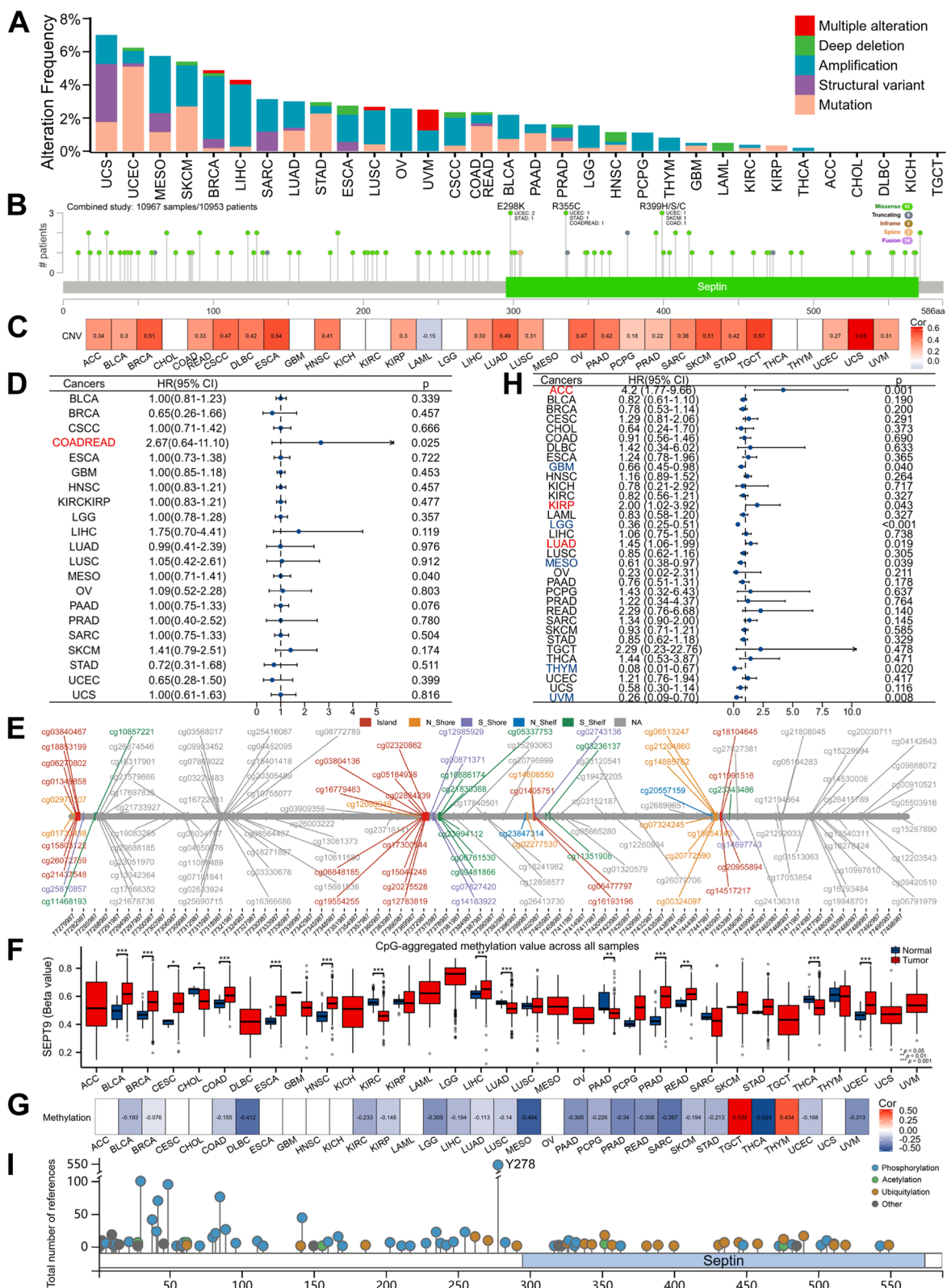Wang *et al. BMC Cancer* (2024) 24:1105

Page 8 of 20

Fig. 3 (See legend on previous page.)

into seven steps: cancer antigen release, cancer antigen presentation, priming and activation, immune cell recruiting, immune cell infiltration, T cell recognition, and cancer cell killing. *SEPT9* was negatively correlated with the cycles of most cancers, indicating the occurrence of immunosuppression, but was positively correlated with these cycles in KIRC, LAML, LGG, PAAD, PRAD, THCA, and UVM (Fig. 6C; Table S8). Furthermore, we explored the relationship between *SEPT9* and the three clusters of immunoregulators. *SEPT9* was positively correlated with them in most cancers but negatively correlated with MHC molecules in LUSC, MESO, OV, SARC, TGCT, and THYM, immunostimulators in DLBC, GBM, LUSC, SARC, SKCM, and THYM, and immunoinhibitors in DLBC, GBM, LUSC, SARC, TGCT, and THYM. In particular, its correlation with immunoinhibitors may become a key target for immunotherapy (Fig. 6D-F; Table S8).

ICB, the most important immunotherapy method, relies mainly on immune cell infiltration and is influenced by the tumor mutation burden (TMB), microsatellite instability (MSI), and tumor stemness. High TMB or MSI scores indicate high immune cell infiltration and vice versa. The results indicated that the correlation between *SEPT9* and TMB was positive in LGG, PAAD, and SKCM but was negative in CESC, PRAD, and THYM. Furthermore, the correlation between *SEPT9* and MSI was positive in CESC, LIHC, LUSC, OV, and UVM but was negative in PCPG, PRAD, and STAD. As tumor stemness is correlated with its metastasis, recurrence, and treatment, we utilized the OCLR algorithm to analyze the correlation between *SEPT9* and tumor stemness. *SEPT9* showed negative correlations with the stemness of the majority of tumors. However, positive correlations with tumor stemness existed in BRCA, SKCM, and THYM, indicating that patients with low *SEPT9* expression exhibited higher tumor stemness compared to those with high expression (Fig. 6G; Table S8). Next, we predicted the treatment impact of ICB and discovered that the low-*SEPT9* group exhibited lower TIDE scores compared to the high-*SEPT9* group, indicating better treatment effectiveness in patients with COAD, ESCA, GBM, HNSC, KIRC, KIRP, LGG, LIHC, LUSC, MESO, PAAD, PCPG, PRAD, READ, STAD, TGCT, and THCA (Fig. 6H).

Additionally, we further studied the relationship between *SEPT9* and drug sensitivity. *SEPT9* was significantly associated with 61 FDA-approved or clinical trial-tested drugs. Specifically, it was negatively correlated with 23 drugs, especially OTS-964, Docetaxel, ARQ-621, and AT-7519 (Cor < -0.35), while positively correlated with other 38 drugs, especially SNS-314, XL-147, Pracinostat, LGK-974, PLX-4720, and Vorinostat (Cor > 0.35), implying that patients with high *SEPT9* expression were particularly sensitive to OTS-964, Docetaxel, ARQ-621, and AT-7519, while they exhibited resistance to SNS-314, XL-147, Pracinostat, LGK-974, PLX-4720, and Vorinostat (Fig. 7A, B; Table S9). To further evaluate the binding affinity between SEPT9 protein and these candidate drugs, we selected OTS-964 (Cor = 0.384) and Vorinostat (Cor = 0.463) for molecular docking with SEPT9. The results indicated that Vorinostat had a strong binding activity with SEPT9 (binding energy: -7.097 kal/mol), while OTS-964 also had a stable binding activity with SEPT9 (binding energy: -6.581 kal/mol) (Fig. 7C). Therefore, *SEPT9* is associated with sensitivity to multiple drugs, making it a promising chemotherapeutic target.

An optimized predictive model was established based on SEPT9 and mitotic spindle genes

Given the prognostic and therapeutic significance of *SEPT9* for LUSC, we attempted to construct a better prognostic model to enhance the prognostic value and improve treatment outcomes. Venn analysis identified 272 shared genes among *SEPT9*-associated genes, DEGs, and prognostic genes (Fig. 8A; Table S10). These genes were used to divide LUSC patients into two clusters (Fig. 8B-D), which were distinguished well by the PCA plot (Fig. 8E). The OS of C1 cluster was worse than that of C2 cluster (Fig. 8F). Analyses of immunoregulator expression in the two clusters revealed that most immunoregulators were more highly expressed in cluster 1 compared to cluster 2, indicating that the overall immune infiltration in the C1 cluster may be enhanced (Fig. 8G).

Previous GSEA analyses showed that *SEPT9*-associated genes were highly enriched in the mitotic spindle gene set. Therefore, we integrated the two gene sets from Hallmark and GO and demonstrated a

---

(See figure on next page.)

Fig. 4 *SEPT9* correlates with clinical factors and is an effective prognostic factor for various cancers, especially LUSC. (**A**) Clinical correlation of *SEPT9* from baseline datasheets. Red and gray boxes represent $p < 0.05$ and $p \geq 0.05$, respectively. (**B**) Clinical correlation of *SEPT9* from bar charts. Red, gray, and blue indicate positive correlation, no significant correlation, and negative correlation, respectively. (**C**) Correlations of *SEPT9* with survival probability. Red and blue boxes indicate risky and protective factors, respectively. (**D**) Violin plot of *SEPT9* expression in normal and LUSC tissue and OS curve of *SEPT9* with GSE19188 dataset. (**E**) OS curves of *SEPT9* with GSE3141 dataset and GSE bulk datasets containing GSE3141, GSE19188, GSE4573, GSE50081, GSE157011, GSE14814, GSE29013, GSE30219, GSE37745 from GEO portal. (**F–H**) Panoramic (**F**), representative (**G**), and statistical graph (**H**) of SEPT9 IHC staining in adjacent and LUSC tissues in microarrays. (**I**) Diagnostic ROC curve of SEPT9 protein. (**J**) Clinical correlation of SETP9 protein with significant differences. (**K**) OS curves of SEPT9 protein
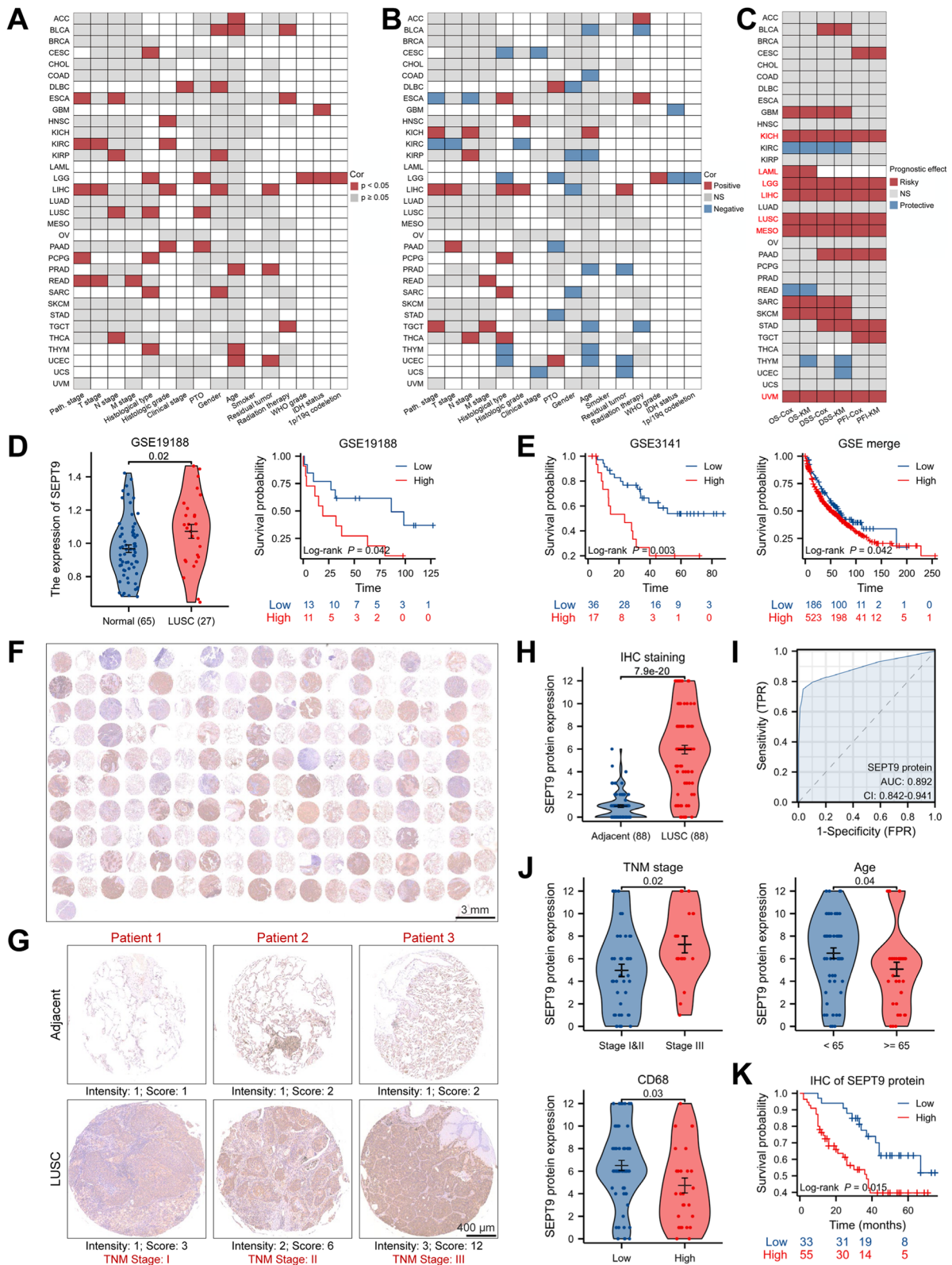
Wang *et al. BMC Cancer*   (2024) 24:1105

Page 10 of 20

Fig. 4 (See legend on previous page.)

Wang *et al. BMC Cancer*   (2024) 24:1105

Page 11 of 20

Table 1 Baseline datasheet of correlation of SEPT9 protein with clinical factors in LUSC

Characteristics	SEPT9-low (33)	SEPT9-high (55)	p
Pathologic grade, n (%)			0.063
Grade II	24 (27.3%)	29 (33%)	
Grade III	9 (10.2%)	26 (29.5%)	
TNM stage, n (%)			0.020
Stage I	8 (12.9%)	8 (12.9%)	
Stage II	15 (24.2%)	12 (19.4%)	
Stage III	3 (4.8%)	16 (25.8%)	
T stage, n (%)			0.106
T2	19 (30.6%)	17 (27.4%)	
T3	6 (9.7%)	14 (22.6%)	
T4	1 (1.6%)	5 (8.1%)	
N stage, n (%)			0.294
N0	18 (21.7%)	24 (28.9%)	
N1	13 (15.7%)	28 (33.7%)	
M stage, n (%)			1.000
M0	32 (36.4%)	54 (61.4%)	
M1	1 (1.1%)	1 (1.1%)	
Gender, n (%)			0.448
Male	33 (37.5%)	52 (59.1%)	
Female	0 (0%)	3 (3.4%)	
Age, n (%)			0.142
> =65	16 (18.2%)	18 (20.5%)	
<65	17 (19.3%)	37 (42%)	
Tumor size, n (%)			0.550
<5 cm	13 (19.7%)	23 (34.8%)	
> =5 cm	13 (19.7%)	17 (25.8%)	
Pathomorphology, n (%)			0.890
Central	19 (45.2%)	16 (38.1%)	
Peripheral	3 (7.1%)	4 (9.5%)	
PD-L1, n (%)			0.013
Low	17 (19.8%)	41 (47.7%)	
High	16 (18.6%)	12 (14%)	
CD8, n (%)			0.783
Low	17 (19.3%)	30 (34.1%)	
High	16 (18.2%)	25 (28.4%)	
CD68, n (%)			0.009
Low	17 (19.3%)	43 (48.9%)	
High	16 (18.2%)	12 (13.6%)	

significant correlation between *SEPT9* and the new gene set (Cor = 0.346, $p < 0.001$) (Fig. 9A; Table S11). Venn analysis was conducted between the 272 cluster genes and the new gene set, resulting in nine prognostic genes (Fig. 9B). Multivariate Cox regression analysis of *SEPT9* and these genes yielded six independent prognostic genes (Fig. 9C), thereby establishing the prognostic risk signature. The equation for risk score was: Risk score $= 0.380 \times SEPT9 + 0.316 \times ARAP3 + 0.356 \times HSF1 + (−0.395) \times FAM83 + (−0.463) \times KIF20B + (−0.349) \times TUBB8$. *SEPT9*, *ARAP3*, and *HSF1* were risk genes, whereas *KIF20B*, *FAM83D*, and *TUBB8* were protective genes (Fig. 9D). The KM plot confirmed that high-risk patients had poorer OS than low-risk patients (Fig. 9E). ROC analysis revealed that the AUCs of 1-, 3-, and 5-year OS were 0.633, 0.712, and 0.679, respectively (Fig. 9F). Clinical factors were then included in the prognostic model. Univariate Cox analysis found that increased risk scores were highly correlated with the malignant progression of LUSC, including pathologic stage III&IV, T3&4, and M1, and with tumor after therapy, but was negatively correlated with short smoke history and progressive or stable disease after primary therapy. Multivariate Cox regression analysis confirmed that only risk score, T stage, smoking history, tumor status, and PTO were independent prognostic factors (Fig. 9G). Based on these factors, we established a nomogram model to predict 1-, 3-, and 5-year survival (Fig. 9H). The prognostic calibration curve and the ideal diagonal matched well, and the concordance (0.755) was also relatively high (Fig. 9I). DCA indicated that the nomogram was an effective prognosticator (Fig. 9J). These results indicated that the constructed model is an excellent indicator of LUSC prognosis.

Moreover, we investigated the relationship of the risk signature with the TIM. Consistent with the previous speculation of immune infiltration between clusters, the immune infiltration in the high- and low-risk groups was reversed, with high-risk patients having higher TME scores than low-risk patients (Fig. 9K, L). However, the TMB and stemness scores of the high-risk group were lower than those of the low-risk group, whereas no significant difference in MSI was observed (Fig. 9M). ICB prediction also showed high consistency with immune infiltration, and that the low-risk group was more effective than the high-risk group (Fig. 9N). Overall, C1 cluster patients had more correlations with the high-risk, high-ESTIMATE, high-TME, and high-TIDE groups, as well as dead status, whereas C2 cluster patients showed the opposite trend (Fig. 9O).

Discussion

Cancer has the highest incidence and mortality rates worldwide, and its etiology and treatment remain a great concern [1]. SEPT9, a member of the fourth cytoskeletal protein family, plays important roles in cytoskeletal assembly and cytoplasmic division. Although its carcinogenicity has received increasing attention, its specific role in various cancers remains unclear.

In the present study, our aim was to explore the impact of *SEPT9* on cancer occurrence and development. To this end, we first conducted expression analysis. In normal
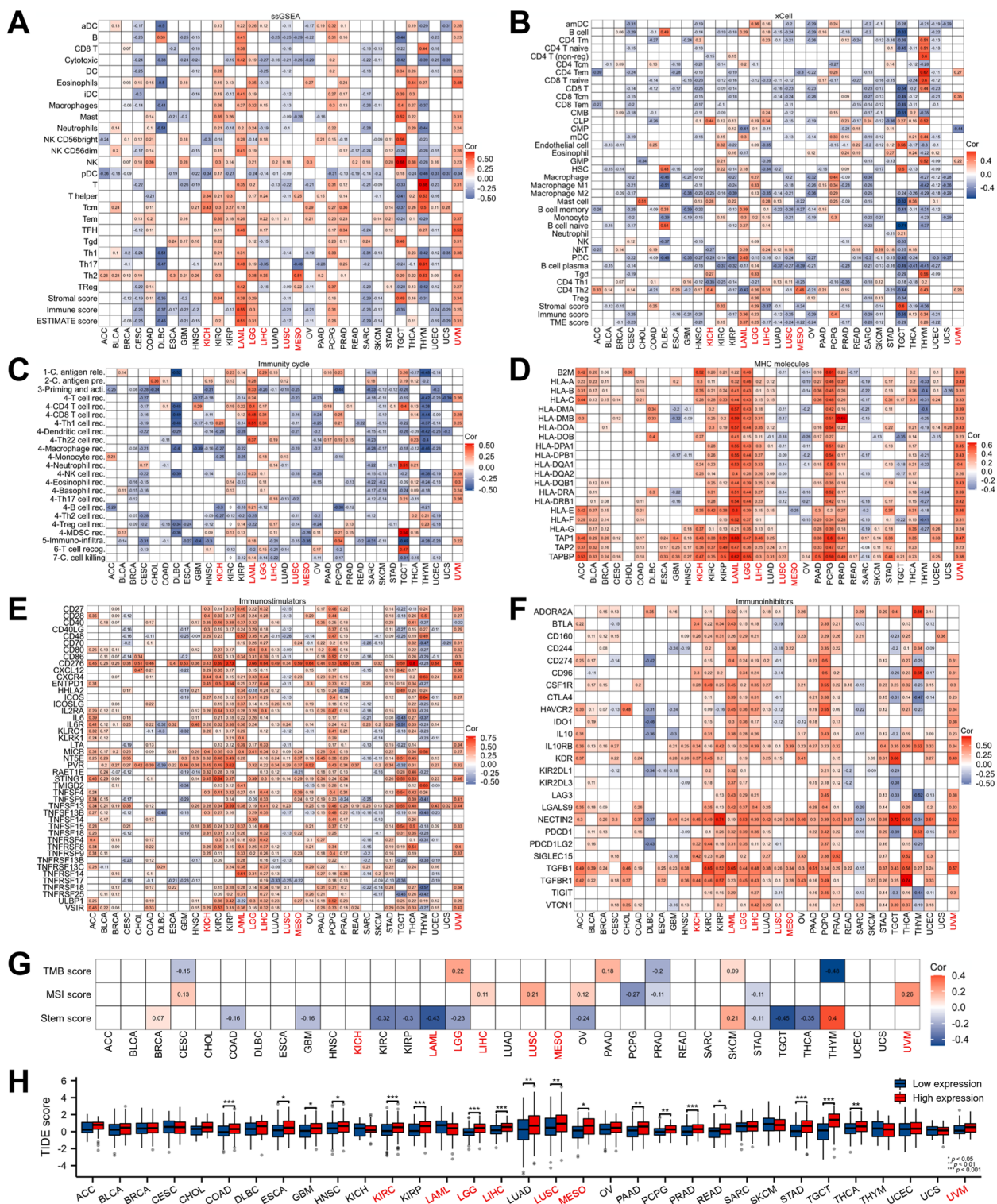
Fig. 5 *SEPT9* is associated with tumor-promoting signature and TIM and is enriched in both malignant and immune cells by functional enrichment and single-cell expression analyses. (**A**) GSEA of *SEPT9*-associated DEGs in hallmarks in pan-cancer. Red and blue boxes represent positive and negative enrichments, respectively. (**B**) Cluster heatmap of *SEPT9* expression in cancers. (**C**) Representative UMAP plots of *SEPT9*-enriched cell clusters in ALL, COADREAD, and Glioma

human tissues, *SEPT9* is highly expressed in lymphoid tissue and bone marrow, which are the most active areas of cell division and are therefore most likely to undergo carcinogenesis. Single-cell sequencing analysis of healthy tissues revealed high enrichments of *SEPT9* in immune cells, suggesting it is involved in immune cell infiltration.

Fig. 6 *SEPT9*-related TIM is beneficial for predicting immunotherapeutic efficacy. (**A, B**) Correlation of *SEPT9* with TME infiltration using the ssGSEA and ESTIMATE (A), as well as xCell (B) algorithms. (**C**) Correlation of *SEPT9* with immunity cycle using TIP portal. (**D-F**) Correlation of *SEPT9* with MHC molecules (**D**), immunostimulators (**E**), and immunoinhibitors (**F**). (**G**) Correlation of *SEPT9* with TMB, MSI, and Stem score. (**H**) Comparison of predicted TIDE score according to *SEPT9* expression using the TIDE algorithm
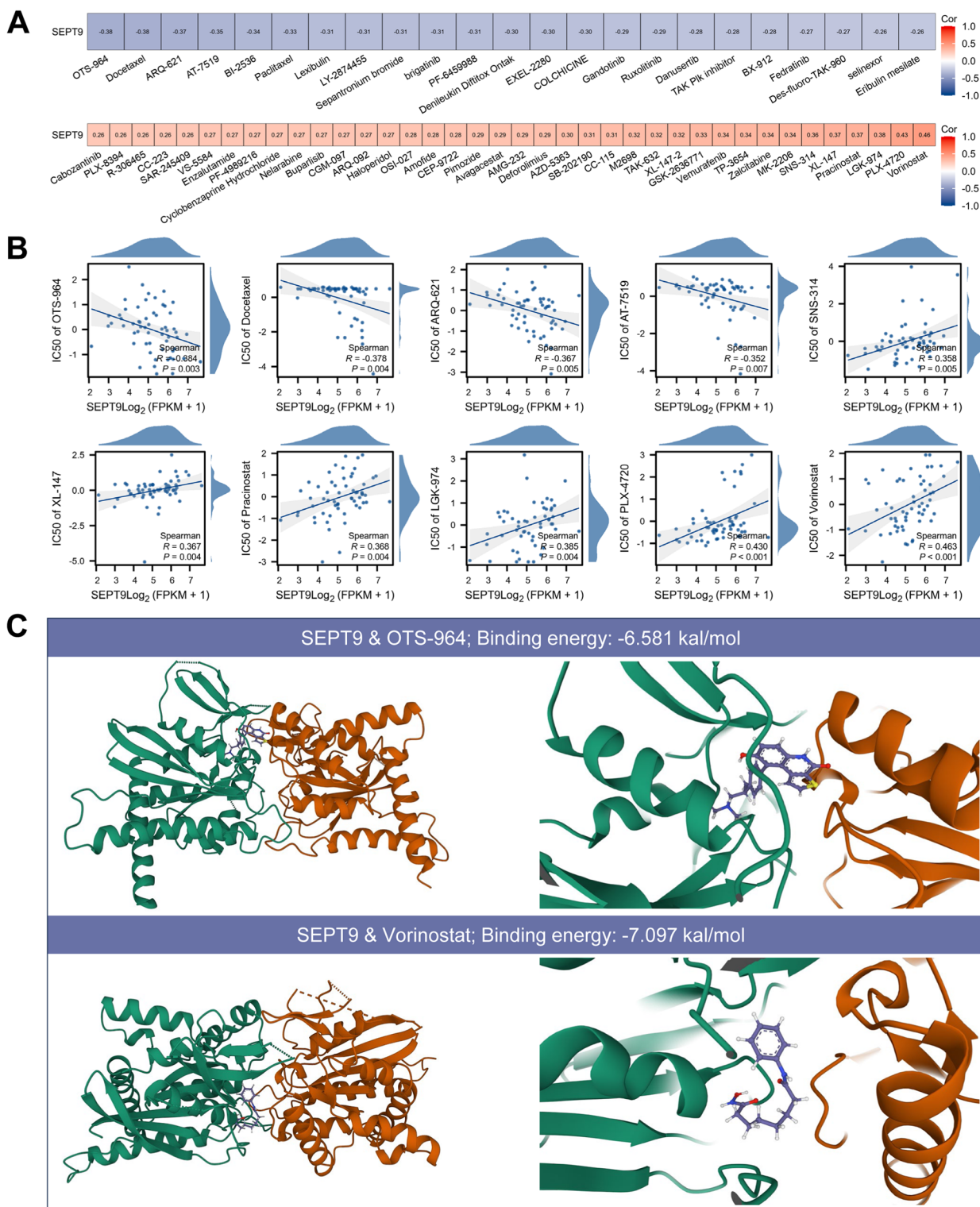
Fig. 7 *SEPT9* is associated with drug sensitivity. (**A**) Correlation of *SEPT9* with IC50 of drug from CellMiner database. (**B**) Scatter plots of the top 10 drugs with the highest correlation with *SEPT9*. (**C**) Molecular docking of SEPT9 protein with the most negative and positive related drugs
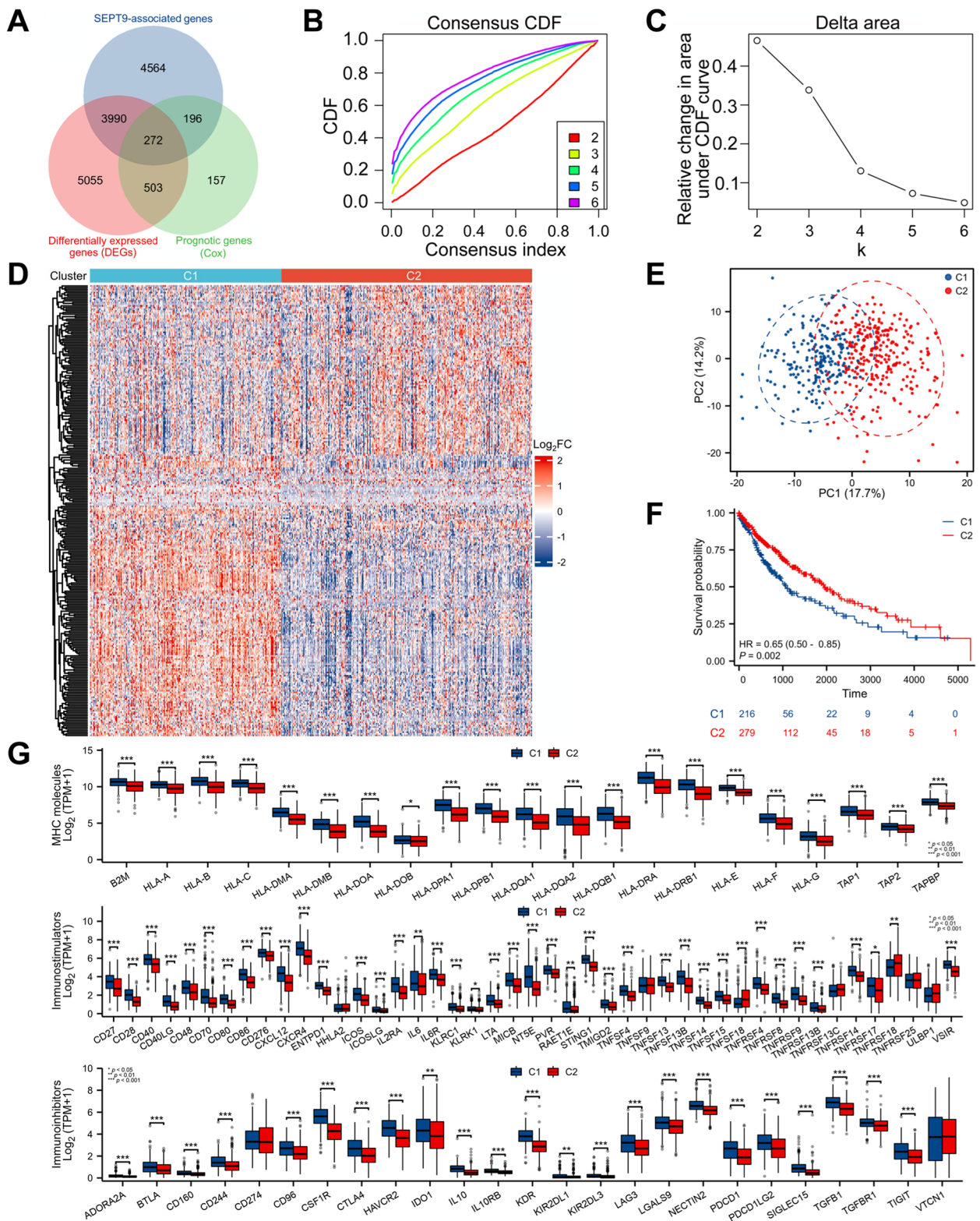
Fig. 8 Identification and evaluation of *SEPT9*-associated prognostic clusters in LUSC. (**A**) Venn analysis of *SEPT9*-associated genes, DEGs, and prognostic OS genes. (**B**) Consensus CDF curve. (**C**) Relative area changes. (**D**) Differential expression of genes in two clusters. (**E**) PCA plot. (**F**) OS curve. (**G**) Comparison of immunoregulators expression between two clusters, including MHC molecules, immunostimulators, and immunoinhibitors

Comparison of normal and tumor tissues revealed that *SEPT9* was highly expressed in most tumor tissues and was associated with multiple clinical factors, demonstrating its prognostic value for various cancers, including KICH, LAML, LGG, LIHC, LUSC, MESO, and UVM. Furthermore, we confirmed that high *SEPT9* mRNA and protein expression can serve as good diagnostic and prognostic indicators for LUSC.

We further explored the possible mechanism by which *SEPT9* causes prognostic differences with functional enrichment and single-cell expression analysis of tumor tissues. *SEPT9*-associated DEGs correlated with various cancer-promoting and immune-related signatures, and *SEPT9* was widely enriched in malignant and immune cells, especially in the latter, suggesting its important role in tumor development, immune infiltration, and immunotherapy. An increasing number of studies have linked *SEPTs* with TIM infiltration. For example, *SEPT2* knockdown inhibits Fc receptor-mediated phagocytosis in HeLa cells and macrophages, increases the permeability of human bronchial epithelial and endothelial cells, and accelerates leukocyte migration and thrombin-induced barrier disruption [34–37]. Meanwhile, *SEPT7* knockout suppresses mouse T-cell migration and increases the permeability of human colon epithelial cells [38]. Knockout of *SEPT7* or *SEPT9* inhibits T cell proliferation in mice, thereby reducing the number of mature T cells [39–42]. In the present study, we found that *SEPT9*-related TIM was exceptionally complex, as *SEPT9* not only positively or negatively correlated with two immune cell types with opposite functions in the same tumor, but also consistently correlated with immune-promoting and-suppressive factors. Increased *SEPT9* expression promoted immune infiltration in KIRC, LAML, LGG, PCPG, THCA, THYM, and UVM and inhibited immune infiltration in BRCA, CESC, DLBC, GBM, HNSC, LIHC, LUAD, LUSC, MESO, OV, PRAD, SARC, SKCM, TGCT, UCEC, and UCS. Therefore, in tumors wherein *SEPT9* and TIM are positively correlated, ICB treatment was more effective in suppressing immune checkpoints of the low-*SEPT9* group than of the high-*SEPT9* group. In addition, *SEPT9* and the IC50 of drugs were correlated, particularly Vorinostat and OTS-964. High *SEPT9* expression

was sensitive to OTS-964, while it exhibited resistance to Vorinostat. Molecular docking showed strong binding activity between SEPT9 and Vorinostat, and stable binding with OTS-964. These results indicated that *SEPT9* can serve as a potential target of these drugs, helping predict chemotherapy sensitivity and resistance. Our research reveals the potential for targeting the fourth cytoskeleton represented by *SEPT9* as a novel and effective cancer treatment strategy.

As the recently released global cancer statistics remind us of the urgent need for research in and treatment of lung cancer, we continue to explore the *SEPT9*-associated prognostic model for LUSC to improve their prognostic performance and treatment efficacy [1]. Functional enrichment analysis mentioned that *SEPT9*-associated DEGs were the most enriched mitotic spindle genes. The precise assembly of the mitotic spindle is crucial for ensuring the equal distribution of chromosomes between two daughter cells and plays an indispensable role in maintaining genomic stability [43]. Currently, only two reports have described the role of the mitotic spindle signature in LUAD using bioinformatics [44, 45]. Our study is the first to apply the mitotic spindle prognostic signature, which includes *SEPT9*, *HSF1*, *ARAP3*, *KIF20B*, *FAM83D*, and *TUBB8*, to LUSC and associate them with clinical factors to obtain a better prognostic model. Heat shock factor protein 1 (*HSF1*), a stress-induced and DNA-binding transcription factor, protects cells from damage and promotes cancer development, including EMT, cancer-related metabolic changes, cancer stemness, and malignant transformation, and is associated with the deterioration of the condition of cancer patients [46–48]. Arf-GAP with Rho-GAP domain, ANK repeat and PH domain-containing protein 3 (*ARAP3*) is a GTPase-activating protein that regulates actin cytoskeleton remodeling. During gastric cancer development, ARAP3 affects cell invasion by regulating cell adhesion and motility, thereby inhibiting the peritoneal spread of refractory cancer cells [49]. *ARAP3* may also be a prognostic factor of breast cancer and SARC, which are related to breast metastasis and the immune infiltration of SARC

(See figure on next page.)

Fig. 9 Establishment and evaluation of *SEPT9* and mitotic spindle-associated nomogram based on the clusters in LUSC. (**A**) Correlation of *SEPT9* and mitotic spindle genes. (**B**) The Venn diagram of *SEPT9*-associated differentially expressed prognostic genes and mitotic spindle genes. (**C**) Constructing prognostic risk from selected nine genes using multivariate Cox regression of OS. (**D**) Prognostic risk factor plot of six genes. (**E**) OS curve. (**F**) Time-dependent ROC curve. (**G**) Uni- and multi-variate Cox analyses of risk scores and clinical factors. (**H**) Construction of OS nomogram with independent prognostic factors. (**I**) Prognostic calibration analysis. (**J**) DCA plots. (**K, L**) Comparison of TIM infiltration between risk groups. (**M**) Comparison of TMB, MSI, and Stem scores between risk groups. (**N**) Comparison of TIDE scores from ICB therapy. (**O**) Sankey diagram of the relationship among the clusters, risk scores, ESTIMATE score, TME score, TIDE score, and survival status
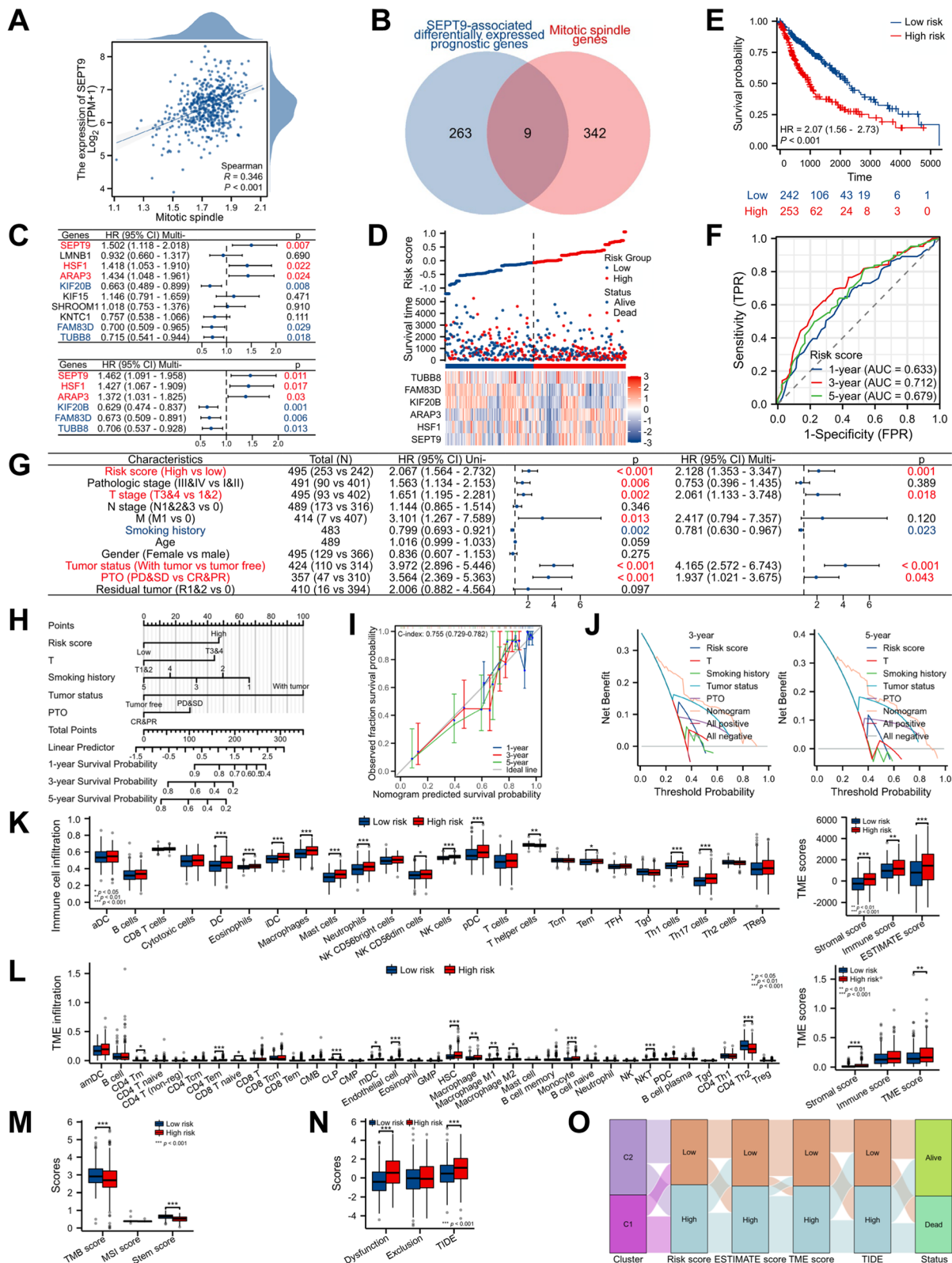
Fig. 9 (See legend on previous page.)

Wang *et al. BMC Cancer*   (2024) 24:1105

Page 18 of 20

[50, 51]. Kinesin-like protein KIF20B (*KIF20B*) is a plus-end-directed motor enzyme required for cytokinesis, which promotes cancer cell proliferation and inhibits apoptosis [52–56]. *FAM83D* inhibits tumor cell autophagy and promotes proliferation, EMT, migration, and invasion by activating ERK1/ERK2 signaling, inhibiting MTOR, JUN, and MYC signaling, and recruiting KIF22 to mitotic spindle [57–59]. *TUBB8* is a basic component of microtubules and plays crucial roles in meiotic spindle assembly and oocyte maturation. However, its association with cancer has not been reported yet [60].

Interestingly, a comparison of our prognostic model with *SEPT9* expression alone revealed a shift in the correlation between our constructed model and TIM, which can better explain the choice of ICB treatment patients. Specifically, *SEPT9* and TIM were negatively correlated in LUSC, but ICB treatment was more effective for the low-*SEPT9* group. As per our model, the immune infiltration in the high-risk group was stronger than that in the low-risk group, thus TIM was more beneficial for patient recovery in the high-risk group, while ICB treatment was more effective for the low-risk population.

Inevitably, there are also certain shortcomings in this study. Although we used tissue microarray to validate the diagnostic and prognostic significance of *SEPT9* in LUSC, further research has not been conducted on other prognostic-related cancers, especially gliomas, as reports have suggested that abnormal expression and mutations in *SEPT9* are associated with neurological diseases, and drug research targeting SEPTs provides new effective treatment strategies for neurodegenerative diseases [61–66]. Moreover, our research lacked systematic research on the *SEPT* family, particularly regarding their functional complementarity in tumorigenesis and clinical practice. Therefore, larger-scale basic experiments in vivo and in vitro are needed in the future to determine the specific molecular mechanisms of *SEPT9* and its family affecting cancer occurrence and development, as well as to conduct clinical sample studies at the pan-cancer levels.

Conclusions
Our study demonstrates that *SEPT9* is a potential pan-cancer screening and prognostic biomarker associated with TIM, providing a new target for immunotherapy and drug therapy. We applied the mitotic spindle prognostic model to LUSC for the first time, which not only enhanced its predictive value but also reshaped the immune microenvironment, making immunotherapy more effective for LUSC patients.

Supplementary Information
The online version contains supplementary material available at https://doi.org/10.1186/s12885-024-12877-4.

Addtional file 1: Fig. S1. The transcripts of human *SEPT9* and protein expression inconsistent with mRNA expression in several tumors. Fig. S2. The prognostic role of *SEPT9* in pan-cancer with TCGA datasets. Fig. S3. Clinical correlation of SETP9 protein with no significant difference.

Additional file 2: Table S1. Correlations of *SEPT9* with CNVs in pan-cancer from cBioPortal (TCGA, PanCancer). Table S2. Correlations of *SEPT9* with CpG-aggregated methylation in pan-cancer from SMART portal. Table S3. Significance of clinical correlation of *SEPT9* using baseline datasheets in pan-cancer from TCGA database. Table S4. Significance of clinical correlation of *SEPT9* using bar charts in pan-cancer from TCGA database. Table S5. Survival probability of different *SEPT9* expression in pan-cancer from TCGA database. Table S6. GSEA of *SEPT9*-associated DEGs in hallmarks in pan-cancer from TCGA database. Table S7. Single-cell expression of *SEPT9* in pan-cancer from GEO database. Table S8. Correlations of *SEPT9* with TIM, immune cycles, immunoregulators, TMB, MSI, and stemness in pan-cancer from TCGA database. Table S9. Correlations of *SEPT9* with IC50 of drugs from CellMiner database. Table S10. Genes for screening *SEPT9*-associated prognostic clusters. Table S11. Mitotic spindle genes from MSigDB portal.

Declarations

Ethics approval and consent to participate
The study was approved by the Ethics Committee of Shanghai Qutdo Biotechnology Company, and received informed consent from all participants.

Consent for publication
Not Applicable.

Competing interests
The authors declare no competing interests.

Author details
[1]Translational Medicine Research Center, Key Laboratory of Clinical Cancer Pharmacology and Toxicology Research of Zhejiang Province, Affiliated Hangzhou First People's Hospital, School of Medicine, Westlake University, Hangzhou 310006, Zhejiang, China. [2]Department of Medical Oncology, The First

Wang *et al. BMC Cancer*   (2024) 24:1105

Page 19 of 20

Affiliated Hospital, Zhejiang University School of Medicine, Hangzhou 310006, Zhejiang, China. ³Key Laboratory of Bio-Medical Diagnostics, Suzhou Institute of Biomedical Engineering and Technology, Chinese Academy of Sciences, Suzhou 215163, Jiangsu, China. ⁴Department of the Fourth Clinical Medical College, Zhejiang Chinese Medical University, Hangzhou 310006, Zhejiang, China. ⁵Department of Oncology, Hangzhou Cancer Hospital, Hangzhou 310006, Zhejiang, China.

References

1. Bray F, Laversanne M, Sung H, Ferlay J, Siegel RL, Soerjomataram I, Jemal A. Global cancer statistics 2022: GLOBOCAN estimates of incidence and mortality worldwide for 36 cancers in 185 countries. CA Cancer J Clin. 2024;74(3):229–63.
2. Swanton C, Bernard E, Abbosh C, Andre F, Auwerx J, Balmain A, Bar-Sagi D, Bernards R, Bullman S, DeGregori J, et al. Embracing cancer complexity: Hallmarks of systemic disease. Cell. 2024;187(7):1589–616.
3. Yuan S, Almagro J, Fuchs E. Beyond genetics: driving cancer with the tumour microenvironment behind the wheel. Nat Rev Cancer. 2024;24(4):274–86.
4. Rosic G. Cancer signaling, cell/gene therapy, diagnosis and role of nanobiomaterials. Adv BiolEarth Sci. 2024;9(Special Issue):11–34.
5. Weirich CS, Erzberger JP, Barral Y. The septin family of GTPases: architecture and dynamics. Nat Rev Mol Cell Biol. 2008;9(6):478–89.
6. Buckley CE, St Johnston D. Apical-basal polarity and the control of epithelial form and function. Nat Rev Mol Cell Biol. 2022;23(8):559–77.
7. Neubauer K, Zieger B. The Mammalian Septin Interactome. Front Cell Dev Biol. 2017;5:3.
8. Spiliotis ET, Nakos K. Cellular functions of actin- and microtubule-associated septins. Curr Biol. 2021;31(10):R651–66.
9. Angelis D, Spiliotis ET. Septin Mutations in Human Cancers. Front Cell Dev Biol. 2016;4:122.
10. Pous C, Klipfel L, Baillet A. Cancer-Related Functions and Subcellular Localizations of Septins. Front Cell Dev Biol. 2016;4:126.
11. Sun J, Zheng MY, Li YW, Zhang SW. Structure and function of Septin 9 and its role in human malignant tumors. World J Gastrointest Oncol. 2020;12(6):619–31.
12. Osaka M, Rowley JD, Zeleznik-Le NJ. MSF (MLL septin-like fusion), a fusion partner gene of MLL, in a therapy-related acute myeloid leukemia with a t(11;17)(q23;q25). Proc Natl Acad Sci U S A. 1999;96(11):6428–33.
13. Toth K, Galamb O, Spisak S, Wichmann B, Sipos F, Valcz G, Leiszter K, Molnar B, Tulassay Z. The influence of methylated septin 9 gene on RNA and protein level in colorectal cancer. Pathol Oncol Res. 2011;17(3):503–9.
14. Scott M, McCluggage WG, Hillan KJ, Hall PA, Russell SE. Altered patterns of transcription of the septin gene, SEPT9, in ovarian tumorigenesis. Int J Cancer. 2006;118(5):1325–9.
15. Connolly D, Yang Z, Castaldi M, Simmons N, Oktay MH, Coniglio S, Fazzari MJ, Verdier-Pinard P, Montagna C. Septin 9 isoform expression, localization and epigenetic changes during human and mouse breast cancer progression. Breast Cancer Res. 2011;13(4):R76.
16. Amir S, Wang R, Matzkin H, Simons JW, Mabjeesh NJ. MSF-A interacts with hypoxia-inducible factor-1alpha and augments hypoxia-inducible factor transcriptional activation to affect tumorigenicity and angiogenesis. Cancer Res. 2006;66(2):856–66.
17. Gonzalez ME, Makarova O, Peterson EA, Privette LM, Petty EM. Up-regulation of SEPT9_v1 stabilizes c-Jun-N-terminal kinase and contributes to its pro-proliferative activity in mammary epithelial cells. Cell Signal. 2009;21(4):477–87.
18. deVos T, Tetzner R, Model F, Weiss G, Schuster M, Distler J, Steiger KV, Grutzmann R, Pilarsky C, Habermann JK, et al. Circulating methylated SEPT9 DNA in plasma is a biomarker for colorectal cancer. Clin Chem. 2009;55(7):1337–46.
19. Wang Y, Chen PM, Liu RB. Advance in plasma SEPT9 gene methylation assay for colorectal cancer early detection. World J Gastrointest Oncol. 2018;10(1):15–22.
20. Saeki I, Suehiro Y, Yamauchi Y, Hoshida T, Tanabe N, Oono T, Kawamoto D, Nishimura T, Matsumoto T, Ishikawa T, et al. Methylated SEPT9 assay-based liquid biopsy as a biomarker in molecular targeted agent-treated hepatocellular carcinoma. Hepatol Int. 2023;17(5):1289–99.
21. Grossi I, Assoni C, Lorini L, Smussi D, Gurizzan C, Grisanti S, Paderno A, Mattavelli D, Piazza C, Pelisenco IA, et al. Evaluation of DNA methylation levels of SEPT9 and SHOX2 in plasma of patients with head and neck squamous cell carcinoma using droplet digital PCR. Oncol Rep. 2024;51(3):52.
22. Zhang SL, Yu HJ, Lian ZQ, Wan J, Xie SM, Lei W, Chen QP, Zhang L, Wang Q. Septin9 DNA methylation is associated with breast cancer recurrence or metastasis. J Int Med Res. 2024;52(1):3000605231220827.
23. Cerami E, Gao J, Dogrusoz U, Gross BE, Sumer SO, Aksoy BA, Jacobsen A, Byrne CJ, Heuer ML, Larsson E, et al. The cBio cancer genomics portal: an open platform for exploring multidimensional cancer genomics data. Cancer Discov. 2012;2(5):401–4.
24. Li Y, Ge D, Lu C. The SMART App: an interactive web application for comprehensive DNA methylation analysis and visualization. Epigenetics Chromatin. 2019;12(1):71.
25. Hornbeck PV, Zhang B, Murray B, Kornhauser JM, Latham V, Skrzypek E. PhosphoSitePlus, 2014: mutations, PTMs and recalibrations. Nucleic Acids Res. 2015;43(Database issue):D512-520.
26. Mei J, Cai Y, Xu R, Li Q, Chu J, Luo Z, Sun Y, Shi Y, Xu J, Li D, et al. Conserved immuno-collagenic subtypes predict response to immune checkpoint blockade. Cancer Commun (Lond). 2024;44(5):554–75.
27. Sun D, Wang J, Han Y, Dong X, Ge J, Zheng R, Shi X, Wang B, Li Z, Ren P, et al. TISCH: a comprehensive web resource enabling interactive single-cell transcriptome visualization of tumor microenvironment. Nucleic Acids Res. 2021;49(D1):D1420–30.
28. Xu L, Deng C, Pang B, Zhang X, Liu W, Liao G, Yuan H, Cheng P, Li F, Long Z, et al. TIP: A Web Server for Resolving Tumor Immunophenotype Profiling. Cancer Res. 2018;78(23):6575–80.
29. Wang Q, Li M, Yang M, Yang Y, Song F, Zhang W, Li X, Chen K. Analysis of immune-related signatures of lung adenocarcinoma identified two distinct subtypes: implications for immune checkpoint blockade therapy. Aging (Albany NY). 2020;12(4):3312–39.
30. Jiang P, Gu S, Pan D, Fu J, Sahu A, Hu X, Li Z, Traugh N, Bu X, Li B, et al. Signatures of T cell dysfunction and exclusion predict cancer immunotherapy response. Nat Med. 2018;24(10):1550–8.
31. Reinhold WC, Sunshine M, Liu H, Varma S, Kohn KW, Morris J, Doroshow J, Pommier Y. Cell Miner: a web-based suite of genomic and pharmacologic tools to explore transcript and drug patterns in the NCI-60 cell line set. Cancer Res. 2012;72(14):3499–511.
32. Morris GM, Huey R, Olson AJ: Using AutoDock for ligand-receptor docking. *Curr Protoc Bioinformatics* 2008, Chapter 8:Unit 8 14.
33. Angerani S, Lindberg E, Klena N, Bleck CKE, Aumeier C, Winssinger N. Kinesin-1 activity recorded in living cells with a precipitating dye. Nat Commun. 2021;12(1):1463.
34. Huang YW, Yan M, Collins RF, Diciccio JE, Grinstein S, Trimble WS. Mammalian septins are required for phagosome formation. Mol Biol Cell. 2008;19(4):1717–26.
35. Amado-Azevedo J, de Menezes RX, van Nieuw Amerongen GP, van Hinsbergh VWM, Hordijk PL. A functional siRNA screen identifies RhoGTPase-associated genes involved in thrombin-induced endothelial permeability. PLoS ONE. 2018;13(7):e0201231.
36. Kim J, Cooper JA. Septins regulate junctional integrity of endothelial monolayers. Mol Biol Cell. 2018;29(13):1693–703.
37. Sidhaye VK, Chau E, Breysse PN, King LS. Septin-2 mediates airway epithelial barrier function in physiologic and pathologic conditions. Am J Respir Cell Mol Biol. 2011;45(1):120–6.
38. Sun L, Cao X, Lechuga S, Feygin A, Naydenov NG, Ivanov AI. A Septin Cytoskeleton-Targeting Small Molecule, Forchlorfenuron, Inhibits Epithelial Migration via Septin-Independent Perturbation of Cellular Signaling. Cells. 2019;9(1):84.
39. Lassen LB, Fuchtbauer A, Schmitz A, Sorensen AB, Pedersen FS, Fuchtbauer EM. Septin9 is involved in T-cell development and CD8+ T-cell homeostasis. Cell Tissue Res. 2013;352(3):695–705.
40. Mujal AM, Gilden JK, Gerard A, Kinoshita M, Krummel MF. A septin requirement differentiates autonomous and contact-facilitated T cell proliferation. Nat Immunol. 2016;17(3):315–22.
41. Ivanov AI, Le HT, Naydenov NG, Rieder F. Novel Functions of the Septin Cytoskeleton: Shaping Up Tissue Inflammation and Fibrosis. Am J Pathol. 2021;191(1):40–51.

Wang *et al. BMC Cancer*   (2024) 24:1105

Page 20 of 20

42. Wang X, Wang W, Wang X, Wang M, Zhu L, Garba F, Fu C, Zieger B, Liu X, Liu X, et al. The septin complex links the catenin complex to the actin cytoskeleton for establishing epithelial cell polarity. J Mol Cell Biol. 2021;13(6):395–408.

43. Prosser SL, Pelletier L. Mitotic spindle assembly in animal cells: a fine balancing act. Nat Rev Mol Cell Biol. 2017;18(3):187–201.

44. Shen R, Li Z, Wu X. The mitotic spindle-related seven-gene predicts the prognosis and immune microenvironment of lung adenocarcinoma. J Cancer Res Clin Oncol. 2023;149(12):10131–41.

45. Zhang L, He M, Zhu W, Lv X, Zhao Y, Yan Y, Li X, Jiang L, Zhao L, Fan Y, et al. Identification of a panel of mitotic spindle-related genes as a signature predicting survival in lung adenocarcinoma. J Cell Physiol. 2020;235(5):4361–75.

46. Chen F, Fan Y, Cao P, Liu B, Hou J, Zhang B, Tan K. Pan-Cancer Analysis of the Prognostic and Immunological Role of HSF1: A Potential Target for Survival and Immunotherapy. Oxid Med Cell Longev. 2021;2021:5551036.

47. Chin Y, Gumilar KE, Li XG, Tjokroprawiro BA, Lu CH, Lu J, Zhou M, Sobol RW, Tan M. Targeting HSF1 for cancer treatment: mechanisms and inhibitor development. Theranostics. 2023;13(7):2281–300.

48. Cyran AM, Zhitkovich A. Heat Shock Proteins and HSF1 in Cancer. Front Oncol. 2022;12:860320.

49. Yagi R, Tanaka M, Sasaki K, Kamata R, Nakanishi Y, Kanai Y, Sakai R. ARAP3 inhibits peritoneal dissemination of scirrhous gastric carcinoma cells by regulating cell adhesion and invasion. Oncogene. 2011;30(12):1413–21.

50. Han JJ, Du BR, Zhang CH. Bioinformatic analysis of prognostic value of ARAP3 in breast cancer and the associated signaling pathways. Eur Rev Med Pharmacol Sci. 2017;21(10):2405–12.

51. Wang Y, Jiang R, Wang T, Wu Z, Gong H, Cai X, Liu J, Yang X, Wei H, Jiao J, et al. Identification of ARAP3 as a regulator of tumor progression, macrophage infiltration and osteoclast differentiation in a tumor microenvironment-related prognostic model of Ewing sarcoma. Am J Cancer Res. 2023;13(8):3721–40.

52. Janisch KM, McNeely KC, Dardick JM, Lim SH, Dwyer ND. Kinesin-6 KIF20B is required for efficient cytokinetic furrowing and timely abscission in human cells. Mol Biol Cell. 2018;29(2):166–79.

53. Mbugua RW, Takano A, Tsevegjav B, Yokose T, Yamashita T, Miyagi Y, Daigo Y. Characterization of KIF20B as a novel prognostic biomarker and therapeutic target for breast cancer. Int J Oncol. 2024;64(4):43.

54. Lin WF, Lin XL, Fu SW, Yang L, Tang CT, Gao YJ, Chen HY, Ge ZZ. Pseudopod-associated protein KIF20B promotes Gli1-induced epithelial-mesenchymal transition modulated by pseudopodial actin dynamic in human colorectal cancer. Mol Carcinog. 2018;57(7):911–25.

55. Li G, Xie ZK, Zhu DS, Guo T, Cai QL, Wang Y. KIF20B promotes the progression of clear cell renal cell carcinoma by stimulating cell proliferation. J Cell Physiol. 2019;234(9):16517–25.

56. Kanehira M, Katagiri T, Shimo A, Takata R, Shuin T, Miki T, Fujioka T, Nakamura Y. Oncogenic role of MPHOSPH1, a cancer-testis antigen specific to human bladder cancer. Cancer Res. 2007;67(7):3276–85.

57. Santamaria A, Nagel S, Sillje HHW, Nigg EA. The spindle protein CHICA mediates localization of the chromokinesin Kid to the mitotic spindle. Curr Biol. 2008;18(10):723–9.

58. Fulcher LJ, He Z, Mei L, Macartney TJ, Wood NT, Prescott AR, Whigham AJ, Varghese J, Gourlay R, Ball G, et al. FAM83D directs protein kinase CK1alpha to the mitotic spindle for proper spindle positioning. EMBO Rep. 2019;20(9):e47495.

59. Geng Y, Liu J, Wang Z, Liu T, Peng X, Huang Y. Systematic analysis of the oncogenic role of FAM83D across cancers based on data mining. Cell Cycle. 2023;22(8):1005–19.

60. Dong J, Jin L, Bao S, Chen B, Zeng Y, Luo Y, Du X, Sang Q, Wu T, Wang L. Ectopic expression of human TUBB8 leads to increased aneuploidy in mouse oocytes. Cell Discov. 2023;9(1):105.

61. Kuhlenbaumer G, Hannibal MC, Nelis E, Schirmacher A, Verpoorten N, Meuleman J, Watts GD, De Vriendt E, Young P, Stogbauer F, et al. Mutations in SEPT9 cause hereditary neuralgic amyotrophy. Nat Genet. 2005;37(10):1044–6.

62. Sudo K, Ito H, Iwamoto I, Morishita R, Asano T, Nagata K. SEPT9 sequence alternations causing hereditary neuralgic amyotrophy are associated with altered interactions with SEPT4/SEPT11 and resistance to Rho/Rhotekin-signaling. Hum Mutat. 2007;28(10):1005–13.

63. Laccone F, Hannibal MC, Neesen J, Grisold W, Chance PF, Rehder H. Dysmorphic syndrome of hereditary neuralgic amyotrophy associated with a SEPT9 gene mutation–a family study. Clin Genet. 2008;74(3):279–83.

64. Hannibal MC, Ruzzo EK, Miller LR, Betz B, Buchan JG, Knutzen DM, Barnett K, Landsverk ML, Brice A, LeGuern E, et al. SEPT9 gene sequencing analysis reveals recurrent mutations in hereditary neuralgic amyotrophy. Neurology. 2009;72(20):1755–9.

65. Marttinen M, Kurkinen KM, Soininen H, Haapasalo A, Hiltunen M. Synaptic dysfunction and septin protein family members in neurodegenerative diseases. Mol Neurodegener. 2015;10:16.

66. Princen K, Van Dooren T, van Gorsel M, Louros N, Yang X, Dumbacher M, Bastiaens I, Coupet K, Dupont S, Cuveliers E, et al. Pharmacological modulation of septins restores calcium homeostasis and is neuroprotective in models of Alzheimer's disease. Science. 2024;384(6699):eadd6260.

Publisher's Note